Retrieving mean volumetric properties of multiphase flows from 2D images: A new approach combining deep learning algorithms and 3D modelling

Kassem Dia, Fabrice Lamadie, Johan Debayle

Retrieving mean volumetric properties of multiphase flows from 2D images: a new approach combining deep learning algorithms and 3D modelling

Kassem Dia[1,2] , Fabrice Lamadie[1] and Johan Debayle[2]

1 CEA, DES, ISEC, DMRC, Univ Montpellier, Marcoule, France.

2 MINES Saint-Etienne, SPIN/LGF UMR CNRS 5307, 158 cours Fauriel, Saint-Etienne, France.

Contributing authors: kassem.dia@cea.fr; fabrice.lamadie@cea.fr; debayle@emse.fr;

Abstract

Measuring the morphological properties of complex multiphase systems is a crucial problem in many areas of science and industry and is particularly difficult in dense environments with limited optical access. This paper presents a new approach capable of extracting three-dimensional (3D) information from spherical particle systems based solely on two-dimensional (2D) projections of the system. Synthetic images of the system are generated using a stochastic geometrical model from a simulated 3D particle system with the same geometrical features as the studied system, which is projected into 2D images labeled with the appropriate 3D information. These images are then fed to a convolutional neural network (CNN) for training before being tested on synthetic and experimental images. Validation results show that this technique successfully predicts the mean features of the studied systems, even for dense environments with overlapping particles, with high computational efficiency.

Keywords: Convolutional neural network, Particle systems, Stochastic Geometry, 3D Modelling.

1. Introduction

Complex particulate systems are an important and widely studied feature of many industrial processes (Black et al., 1996; Gianinoni et al., 2003; Honkanen et al., 2010) and research projects (Clift, R., Grace, J. R., & Weber, 2005; Poelma, 2020). These systems are generally defined as mixtures of two or more substances where one is suspended in another, either a gas in a liquid (bubble flow) (Juliá et al., 2005; Karn et al., 2015; Lau et al., 2013), a solid in a liquid (Kavanaugh et al., 1980; Yu et al., 2009), or one immiscible liquid in another (emulsions) (Huang et al., 2001; Maaß et al., 2011).

Measuring the properties of these systems is essential to optimize and improve the performance of many processes involving multiphase flows (Emmerich et al., 2019; Panckow et al., 2017). In chemical engineering for example, knowledge of particle spatial distributions is crucial to calculate mass and heat transfer rates and the reaction kinetics governing the efficiency of the process. In this context, the most important properties are the particle size distribution (PSD) of the dispersed field, the mean characteristic diameters ($d_{43}, d_{32}, d_{10}, ...$), the volume fraction of the dispersed phase (ϕ), and morphological information such as the shape and irregularity of the particles.

Extracting this information is a non-trivial problem and many approaches have been investigated in the literature. Laser-based methods involve the analysis of scattered light from a laser beam passing through the system. One of the most popular in-line method is focused beam reflectance measurement (FBRM) (Heath et al., 2002; Ruf et al., 2000), in which a highly focused rotating laser beam is passed at a fixed speed over the suspended particles and the duration of the backscattered light is measured. Although this only provides information on the chord length distribution of the particles, and post processing is required to retrieve the PSD, this technique has successfully been used to measure droplet size distributions in water oil emulsions (Boxall et al., 2010) and micro-bubble size distributions in air flotation processes (Couto et al., 2009), and has proven particularly valuable for the characterization of crystal-like particles (Acevedo et al., 2021; Heinrich and Ulrich, 2012; Pandalaneni and Amamcharla, 2016; Pandit et al., 2019). The second widely used laser-based technique in this context is digital in-line holography (DIH), otherwise known as lens-free imaging (Darakis et al., 2010; Lamadie et al., 2012), in which particle characteristics are estimated from the laser diffraction patterns of the system. This approach has been used to study the position and size of particles in pipe flows (Sentis et al., 2017), microscopic setups (Sheng et al., 2006), and sprays (Yang and Kang, 2011), combined with a machine learning algorithm to study non-uniformly shaped particles (Shao et al., 2020). However, while DIH is very efficient for 3D positioning and PSD measurements, it can only be used in optical dilute media.

Imaging-based methods generally provide richer information than other available techniques and therefore more widely used. Image analysis algorithms combined with direct imaging can be used to measure properties other than the PSD (Maaß et al., 2011), such as the volume fraction of the dispersed phase (Karn et al., 2015), morphological information on irregular particles (Suh et al., 2021), and the presence of clusters (Zhang et al., 2012). The image processing algorithms used have included deterministic methods such as the Hough transform (Yu et al., 2009), watershed segmentation (Chen et al., 2004), more sophisticated approaches to deal with overlapping particles (de Langlard et al., 2018a; Zafari et al., 2020; Zhang et al., 2012; Zou et al., 2021), and recently, machine learning methods (Cui et al., 2022; Haas et al., 2020; Kim and Park, 2021; Li et al., 2021). Most of these techniques extract 2D information from the detection of individual particles and cannot measure 3D properties. Although 3D information can be retrieved from multiple viewpoints, this requires a complex imaging setup with multiple optical access points (Wang et al., 2022; Xue et al., 2014), which is not always desirable or possible.

This article presents a new approach in which a deep learning algorithm is combined with stochastic geometrical models to extract 3D properties from 2D projected images of the system. The 3D stochastic geometrical model is used to generate a huge set of synthetic 2D images labeled with the 3D geometrical properties of the particle field and with the same geometrical properties as experimental images. This model can be used to reproduce any 3D particle field and generate 2D projections suitable to train a convolutional neural network (CNN) (Dia et al., 2022). To the best of our knowledge, this type of approach has only previously been used by Fend et al. (Fend et al., 2021) to reconstruct highly porous 3D structures from focused ion beam scanning electron microscopy data.

The paper is divided into six sections. The following methods section provides a brief reminder of the principles of stochastic geometrical modelling and a description of the chosen machine learning algorithm. The third section describes the parameters chosen to measure the performance of the network and the results of tests on representative simulated flows. The fourth section presents experimental results for 3D dispersed phase volume fractions and PSDs retrieved from highly concentrated particle systems. The results obtained for experimental and liquid-liquid system images are presented in section 5 and the final section is an overall conclusion with perspectives.

Computational methods

As mentioned above, the proposed approach (Figure 1) involves two computational tools, a stochastic geometrical model and a CNN.

For the synthetic images to be representative, the simulated particle system should have the same geometrical properties as the studied system, i.e. be statistically representative of the observed particle field. The 3D stochastic model used to generate the images should consist of a hard-core model of the particles, in this case spherical, that accounts for the statistical properties of the dispersed phase by eliminating all particle-particle and particle-wall interactions. Matérn type II point processes (Matérn, 2014) were therefore chosen to generate the synthetic images.

Matérn type II point processes are derived from an underlying homogeneous Poisson point process in $\mathbb{R}^d$ with intensity λ. A point process is simulated and a thinning rule is applied based on a hard-core distance ($r > 0$)

between the generated points, which removes the last arriving point from any pair of points less than $2r$ apart. This process can be considered a marked point process where the first mark r (constant and positive) represents the hard-core radius and the second mark is the time of arrival of the points modeled using a uniform random variable.

The generation process for the synthetic images thus involves the following steps:

1. Choosing a 3D domain $W = \mathbb{R}^2 \times [0, l]$, where $l > 0$ is the length of the projection direction, consistent with the dimensions of the actual measurement volume.
2. Randomly positioning the particles inside W according to a Poisson point process with intensity λ. Each point is marked with a radius r_i, and a time of birth $t_i, \forall\, i \in \{1, \dots, n_p\}$.
3. Applying two thinning rules: *i)* Matérn's thinning rule, *i.e.* eliminating the last arriving point ($\max(t_1, t_2)$) of pairs (x_1, r_1, t_1) (x_2, r_2, t_2) with $\|x_1 - x_2\|_2 \leq r_1 + r_2$, and *ii)* de Langlard et al.'s thinning rule (de Langlard et al., 2018b) to eliminate particle–boundary interactions by removing points with a probability $1 - \exp\left(-U(x, r, t)\right)$, where $U: W \times \mathbb{R}^+ \times [0,1] \longrightarrow \mathbb{R}^+ \cup \{+\infty\}$ is an interaction function.
4. Projecting the generated 3D particle field orthogonally onto a 2D grid to create a single synthetic image, as shown in Figure 1.

The model generates continuous-valued particles that are later discretized when the synthetic images are generated; the resolution of the images can thus be adjusted as required. The whole process is repeated N times to assemble a training database, and the geometrical properties of each 3D model (size distribution, spatial distribution, etc.) are all stored along with the 2D images (cf. Figure 1, second step). Further details about the stochastic 3D model used here can be found in de Langlard et al. (de Langlard et al., 2018b).

This model can also be used when the distances between points are non-deterministic, and is therefore applicable to real systems. As demonstrated by Stoyan and Stoyan (Stoyan and Stoyan, 1985), the thinning rules are generalizable to cases in which the r marks follow a given probability law, and generalized expressions can always be obtained for distribution parameters such as the retention function and the intensity after thinning. The model can also be extended by changing the shape of the particles.

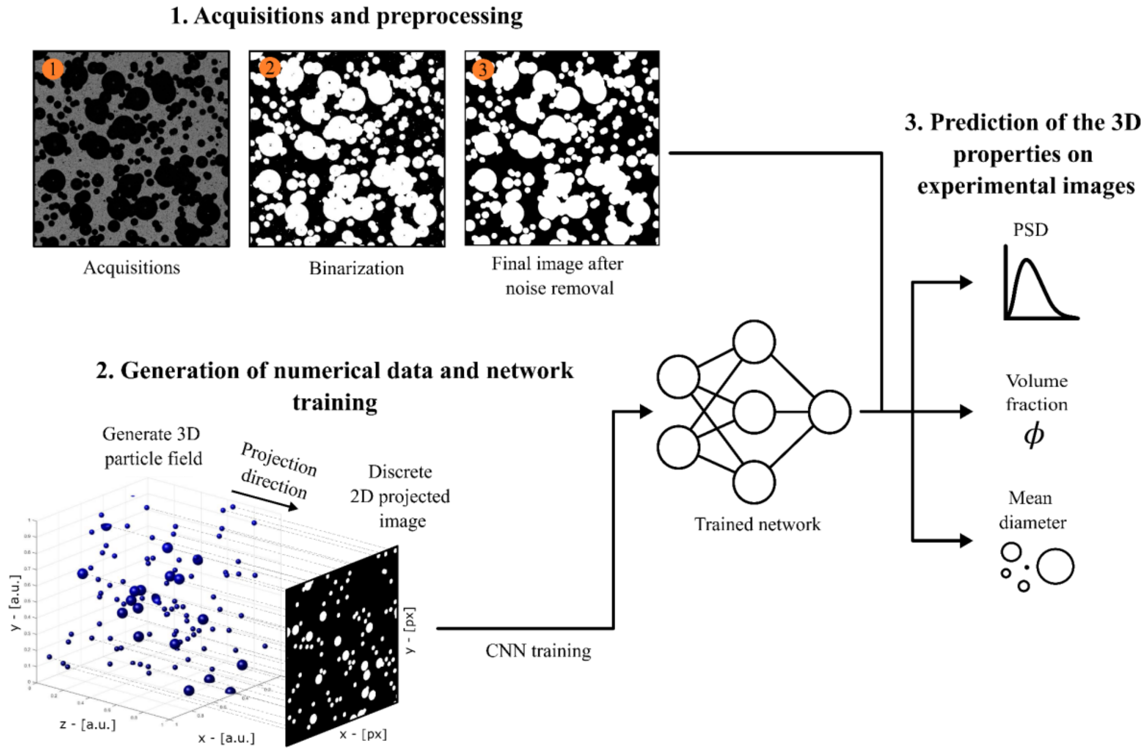

Figure 1. Schematic outline of the main steps of the workflow. 1- Acquisition and preprocessing of experimental images. 2- Generation of a simulated dataset and training of the neural network. 3- Prediction of 3D properties from experimental data.

Note that the training images must be of the same type as the experimental ones, and since a stochastic model is used, only binary images can be used to train the CNN. This means that the experimental data have to be acquired with a backlight setup based on a telecentric lens (cf. section 4) to limit blurring and perspective effects. The images also have to be binarized and denoised before being processed by the CNN (see Figure 1).

The CNN is the second pillar of the proposed approach. Convolutional neural networks are a class of deep learning algorithms designed to process data with a grid-like topology (*e.g.* images, grid cells, financial series…). These algorithms are classed as supervised in the sense that they require both data and labels to be trained to perform a given task. They can be used to solve classification and regression problems but here, only regression CNNs were considered, because the problem involves continuous values.

A CNN broadly consists of four layers (Figure 2):

- An input layer that processes the data provided to the network.

- A feature extraction or convolutional layer, which combines convolutional operations, a non- linear activation function (*e.g.* ReLU, sigmoid), and a pooling operator (*e.g.* max pooling, average pooling) to automatically extract relevant features from the images.
- A fully connected (FC) layer at the end of the network consisting of multiple interconnected neurons whose weights are adjusted to teach the network to identify important features.
- An output layer, which presents the predictions.

Unfortunately, there is no generic way to determine the optimal network shape (*e.g.* the number of convolutional layers, number of neurons, number of layers in the FC layer, the learning rate) in advance. This problem is typically solved using prior experience of CNNs for initial guesses and empirical trials to choose the best architecture. Here, two separate networks were used, one to determine the volume fraction and one to measure the PSD.

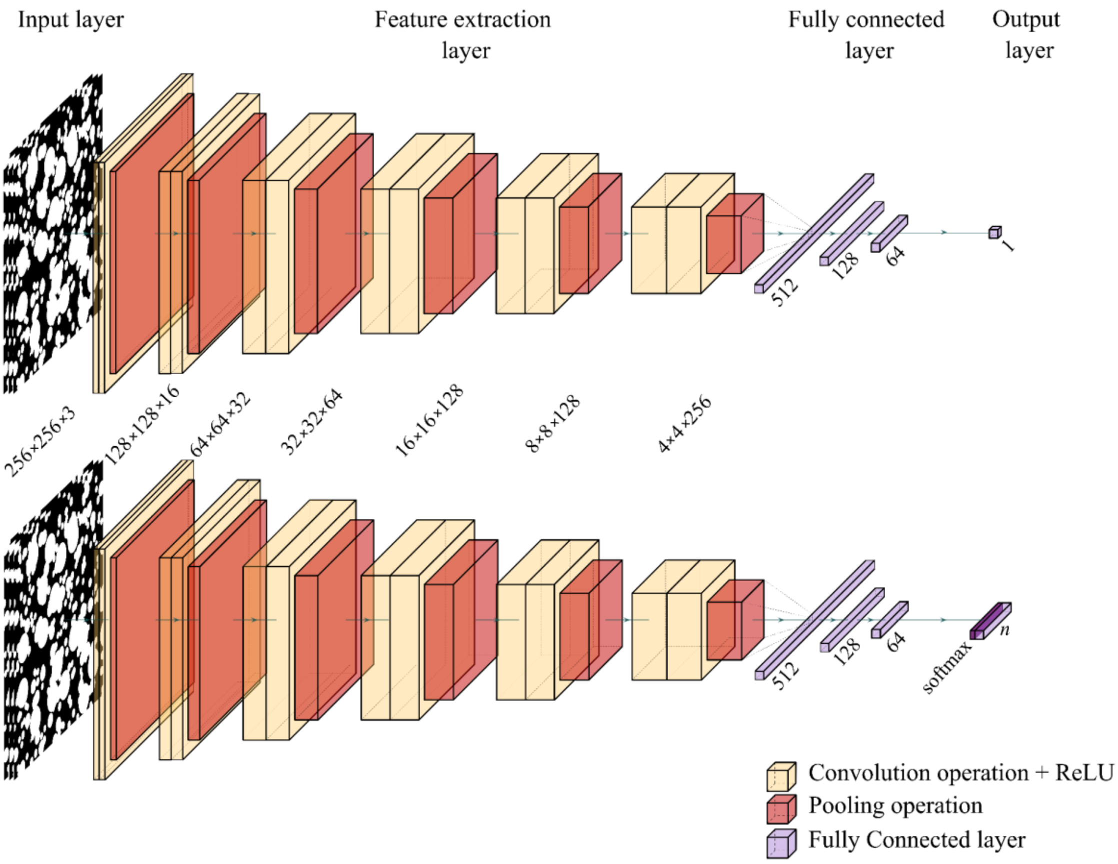

Figure 2. Visualizations of the architectures of the two CNNs used in the study: one to predict the volume fraction (CNN^{Φ}, upper row) used and the other to determine the PSD ($\mathrm{CNN}^{\mathrm{PSD}}$, lower row). The plots were generated with PlotNeuralNet (Iqbal, 2018).

1. The first network, CNN^{ϕ} (Figure 2, top panel) is used to predict the volume fraction (ϕ) of the dispersed phase and was trained on volume-fraction labeled images. The input layer consists of three identical 256×256 images. The feature extraction layer consists of six convolutional layers respectively containing 16, 32, 64, 128, and 256 filters, with a kernel size of 3×3. These layers also contain an activation function, ReLU, are followed by a $2 \times\ 2$ max pooling layer, producing flattened feature maps that are fed to the FC layer. The FC layer contains three sub-layers with 512, 128 and 64 neurons, respectively, and a dropout of 50% is applied after each layer to reduce overfitting. Finally, the output layer consist of a single neuron representing the predicted value, $\hat{\phi}$.
2. The second network, $\mathrm{CNN}^{\mathrm{PSD}}$ (Figure 2, bottom panel), used to predict the 3D PSD, has the same architecture except for the output layer which is a vector of size *n* (note that the output size can be adjusted depending on the studied system). Since the estimated parameter is a distribution, the sum of the elements in the vector is normalized to 1 using the softmax function.

2. Network training strategy

After setting the number of layers and the parameters of the CNN, optimal hyper-parameters were determined by gradient-based optimization. The dataset ($N = 22\ 400$) used to train the network was split into three categories; an initial training set ($N_t = 16\ 000$), a validation set ($N_v = 2\ 000$) used to monitor the overall performance of the network at each iteration, and a final testing set ($N_e = 4\ 400$) used to evaluate the performance of the network. All the generated images corresponded to a measurement volume of $25.79 \times 25.79 \times\ 53$ mm^3 in keeping with the experimental setup. The parameters of the stochastic model were varied uniformly to account for the variety of possible experimental images in real life applications. The intensity of the particles, λ, was adjusted between 100 to 250, while the PSD was modeled as a truncated lognormal function, $\mathcal{L}_{tr}\ (\mu, \sigma^2, a, b)$, with μ varied randomly from -7.5 to 0.06, σ from 0 to 2.5, and a and b equal to 0.005 and 0.08 respectively (check Table 1).

As mentioned above, CNN training datasets have to be labeled with the target information. Here, all the numerical images were generated over a 5.5 h period and each image, *i*, was labeled with the corresponding 3D volume fraction $\phi_i = \frac{v_i}{V_i}$ (with v_i is the volume of the particles, and V_i is total volume) and number weighted PSD (PSD_i) across *n* classes.

Table 1. Details on the synthetic dataset.

	Dataset
#Testing	16000
#Validation	2000
#Testing	4400
ϕ	[0.5 12.2]
Size	$256 \times 256 \times 3$

The hyper-parameters were then optimized using mean absolute error (MAE) as the loss function. The MAE measures the average absolute difference between true $Y = \{y_1, \dots, y_{N_t}\}$ and predicted values $\hat{Y} = \{\hat{y}_1, \dots, \hat{y}_{N_t}\}$:

$$\mathrm{MAE}(Y, \hat{Y}) = \frac{1}{N_t} \sum_{i}^{N_t} |y_i - \hat{y}_i|,$$

Finally, a series of tests were conducted to identify the best number of epochs, the optimal learning rate, and the size of the mini-batches. Slight differences in computational times were observed, so these parameters were optimized as follows:

1. Number of epochs: the CNN was trained using mini-batches due to limited computational resources, with one epoch corresponding to one training run over all the mini-batches. The network training convergence was reached after 100 epochs, therefore the number of epochs was then fixed at 150 with a callback to stop the training run if the MAE increased for 10 straight epochs, to avoid overfitting.
2. Learning rate: The learning rate was adjusted from a starting value of 10^{-4}, with a decay rate of 20% every 50 epochs, down to a final learning rate of 4×10^{-6},
3. Mini-batch size: the mini-batch size was set to 32.

The CNNs were trained using a supercomputer cluster equipped with GPUs each with 640 tensor cores and a memory of 32 GB. The training processes took about 30 min for each CNN.

Since the accuracy of the predictions cannot be determined for regression CNNs, the performance of the networks was determined using the MAE and the relative error (RE) for the volume fraction predictions, and using the MAE only for the PSD. Since the volume fraction is a scalar quantity, MAE calculations are straightforward, but for the PSD, which is a vector, the overall MAE, $\overline{\mathrm{MAE}}$, was calculated by comparing the average values of PSD_i and $\widehat{PSD_i}$.

3. Numerical validation

The performance of CNN^{ϕ} was evaluated using the testing dataset, with hold-up values ranging from 0.5 to 12.2%, and the PSD varied between images.

The results of the predictions compared to the ground truth are shown in Figure 3. The MAE of 0.21 ± 0.26 highlights the overall accuracy of the network's predictions.

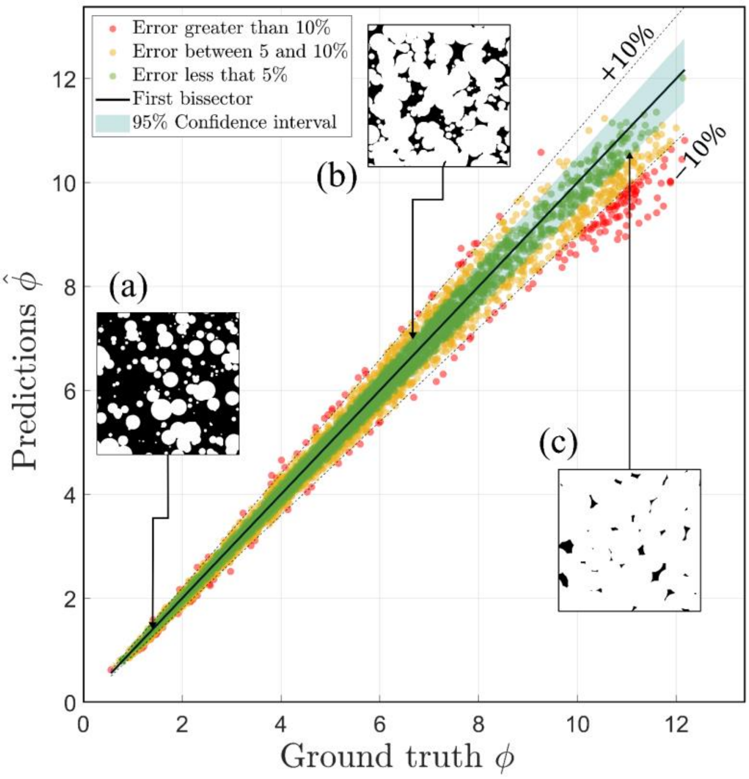

Figure 3. Scatter plot of the predicted 3D volume fraction $\hat{\phi}$ as a function of the ground truth ϕ. The insets show examples of the images from the testing dataset, with $\phi_{(a)} = 1.3\%$, $\phi_{(b)} = 5\%$, and $\phi_{(c)} = 11.3\%$, respectively. The points are color coded according to the relative error of the predictions, $RE_i = \frac{\phi_i - \hat{\phi}_i}{\phi_i}$, green if $|RE_i| \leq 0.05$, orange if $0.05 < |RE_i| \leq 0.1$, and red if $|RE_i| > 0.1$ .The dashed lines border the predictions with less than 10% RE and the first bisector is represented by a solid line. The shaded green area represents the 95% confidence interval of the predictions.

The density of particles in the images naturally increases with the particle volume fraction, making the images more complex to process (compare insets (c) and (a) in Figure 3, for instance). Significant patterns that the network uses to refine its predictions may also disappear. Nevertheless, while the relative errors of the predictions increase with the particle volume fraction, they are all of the correct order of magnitude, confirming the robustness of the approach. Figure 3 shows for instance that below $\phi = 10\%$ (93% occupied area in the images), more than 77% of the network predictions are within the 95% confidence interval.

To validate the PSD estimates, 50 further sets of 100 images were generated using a truncated lognormal function with a fixed particle intensity of $\lambda = 200$. The variance s^2 and the mean diameter $\bar{d}$ were chosen to cover a wide range of narrow and wide unimodal distributions with mean diameters ranging from 500 µm to 5 mm. Predictions were made for each image using the trained $\mathrm{CNN}^{\mathrm{PSD}}$ and binned in 13 size classes. The predictions were then averaged ($\widehat{PSD}$) and compared to the ground truth distribution (PSD) obtained from the corresponding function.

The $\overline{\mathrm{MAE}}$ values obtained (check Table 2) were lower than 0.03 in 60% of the considered cases, corresponding to good agreement between the predicted and ground truth distributions (see Figure 4). For the broadest distributions (variance $\geq 10^{-3}$), corresponding to a maximum occupied surface fraction of about 80%, 82% of the $\overline{\mathrm{MAE}}$ values are less than 0.03. As expected on the other hand, the network performs less well for very narrow distributions (variances range from 10^{-5} to 10^{-4}), as there were no such distributions in the training dataset. The results for four typical cases are presented in Figure 4.

Table 2. Overall MAE for PSD predictions from all 50 simulations. Results for the four cases presented in Figure 4 are highlighted in bold.

Variance s^2 (mm) / Mean $\bar{d}$ (mm)	10^{-5}	10^{-4}	10^{-3}	10^{-2}	10^{-1}
0.5	0.059	0.021	0.009	0.009	**0.009**
1.0	0.085	0.027	0.009	0.009	0.009
1.5	0.071	0.027	0.012	0.010	0.010
2.0	**0.096**	**0.043**	0.014	0.011	0.011
2.5	0.114	0.068	0.018	0.011	0.011
3.0	0.115	0.080	**0.024**	0.013	0.011
3.5	0.123	0.083	0.034	0.014	0.012
4.0	0.115	0.077	0.041	0.015	0.012
4.5	0.114	0.088	0.047	0.018	0.013
5.0	0.131	0.108	0.058	0.022	0.013

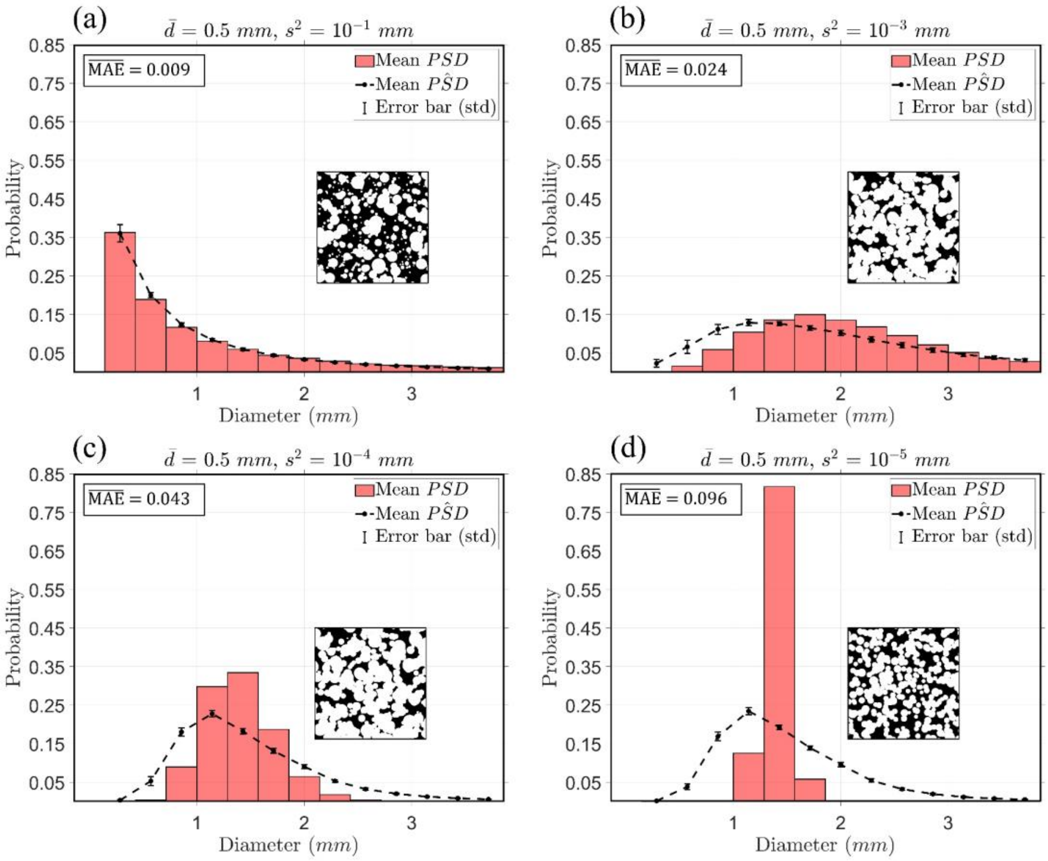

Figure 4. Comparison of CNN^{PSD} predictions with the ground truth for a representative selection of simulated mean particle diameters and particle size variances. The inset in each panel is a typical image of the corresponding particle field. Error bars represent the standard deviations of the predictions.

4. Experimental validation

After validating the approach on simulated data, experimental validations were performed, first using calibrated spherical poly(methyl methacrylate) (PMMA) beads (diameter precision ± 1%) submerged in brine stirred in a rectangular mockup unit and second, using existing data from an emulsion in a cylindrical stirred tank.

4.1.Validation with calibrated beads

Particle suspensions are particularly convenient for validation as they reproduce the main features of two-phase flows but without the coalescence and breakage events that frequently occur with bubbles and droplets. With solid particles moreover, the properties of the dispersed phase are clearly defined. Here, calibrated spherical PMMA particles were stirred in 1 L of brine (330 g NaCl dissolved in 1 L of water) using a four blade propeller.

Brine was chosen so that the density of the continuous phase could be adjusted to that of the dispersed phase to avoid creaming effects and guarantee a homogeneous dispersion of the particles in the flow.

A lognormal distribution of particle sizes cannot be reproduced experimentally using calibrated beads because of time and cost constraints (a 1.48% volume fraction corresponds to about 10000 particles for instance). Therefore, only four sizes of PMMA particles were used (0.39, 0.5, 0.79 and 1.59 mm in diameter), with four volume fractions and a fixed PSD. The number of particles used in each experiment was determined by weighing them with a benchtop precision scale (± 0.2 mg), to evaluate uncertainties on the measured hold-up values. The various experimental configurations are listed in Table 3.

Table **3**. Details of the volume fractions and size distributions used for validation experiments with calibrated bead suspensions.

Experiments	3D hold-up (%)	Size Distribution (PSD)			
	ϕ ($\pm$ scale error)	0.39 mm	0.5 mm	0.79 mm	1.59 mm
1	1.48 ± 0.002	50%	30%	15%	5%
2	2.91 ± 0.003	50%	30%	15%	5%
3	4.31 ± 0.005	50%	30%	15%	5%
4	5.67 ± 0.006	50%	30%	15%	5%

The mixture was placed in a rectangular tank with external dimensions of $25 \times 15 \times 6.7$ cm^3 and a capacity of 1.1 L, fitted with two optical quality windows. The mixture was agitated using a propeller at 2000 rpm to produce a homogenous flow (Figure 5).

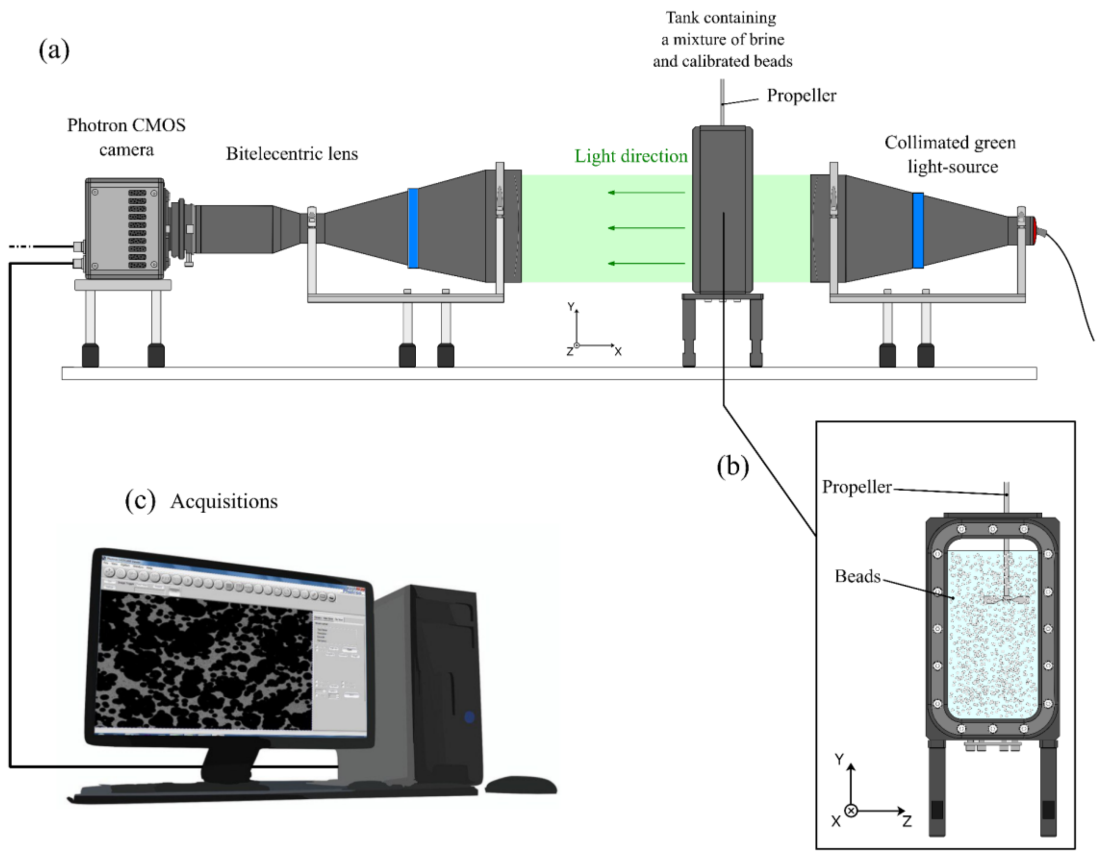

Figure 5. (a) Side-view sketch of the experiment setup with from left to right, the high speed camera, bi-telecentric lens, tank, and collimated green light-source. (b) Front view of the tank. (c) Computer with a typical example of a captured image on the screen ($\phi = 2.91\%$).

Two-dimensional projections of the 3D particle field in the tank were acquired using a backlight setup to avoid perspective effects. A Photron FASTCAM Mini UX100 CMOS camera was attached to an Opto engineering TC16M096 bi-telecentric lens placed 26.2 cm from the center of the tank. The tank and sensor were uniformly illuminated with an Opto engineering collimated green light source (peak wavelength, 525 nm; beam diameter, 120 mm).

The captured images consisted of 1280×1024 squared pixels, corresponding to a field of view of $33.7 \times 29.9\ \mathrm{mm}^2$ (scale factor, 2.6×10^{-2} mm/px). The images were binarized, cropped to 980×980 squared pixels ($25.8 \times 25.8\ \mathrm{mm}^2$), and resized to 256×256 squared pixels to facilitate coding. The tank was 5.3 cm wide along the optical axis and covered the entire telecentric field of view, such that the total measurement volume was 35.3 cm^3. The images were captured at 50 frames per second, with an exposure time of 1/81 920 s, avoiding any motion blur. A set of 4 365 images was acquired for each experiment (Figure 1, first step).

The images underwent three steps of preprocessing, starting with a simple binarization using an arbitrary gray level threshold ($TH = 20$). Morphological area opening using a disk shaped element of 5 pixels was then applied to denoise the images, removing features such as micro bubbles and dust particles, which appear as small white dots in the background. The particle contours were then smoothed using an opening operation (erosion followed by dilatation) with the same structuring element. These morphological operations produce images that are similar to synthetic images (cf. Figure 6). However, small differences between binarized and simulated particles can be observed on pixel-by-pixel inspection. The variance between the images can be quantified using the intersection over union (IoU) ratio between the set of ground truth (synthetic) particles and the set of binarized particles:

$$\mathrm{IoU} = \frac{|A \cap \hat{A}|}{|A \cup \hat{A}|}$$

Where A and $\hat{A}$ stand for the simulated and binarized particles respectively, ∩ and ∪ are respectively the intersection and union operators, and the vertical bars denote cardinality.

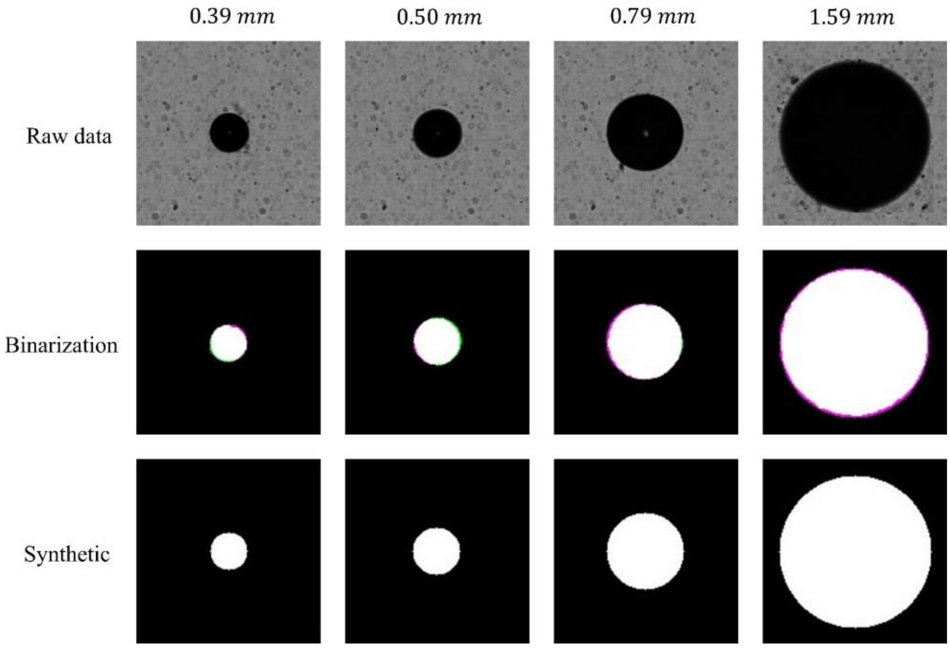

Figure 6. Comparison between binarized raw data ($\hat{A}$) and simulated particles (A). Non-intersecting regions are colored in green for pixels in $\hat{A}$ but not in A and in magenta for pixels in A but not in $\hat{A}$.

The IoU values obtained for all unconnected particles in the dataset (Table 4) show that the discrepancy between the shapes of the modeled particles and real particles is greater for smaller particles. Moreover, Figure 6 shows that while the model underestimates the size of small particles, larger particles are enlarged in the binarized images. Regardless therefore of the training and the architecture of the machine learning network used, discrepancies between the predictions and the ground truth can be expected, especially for the smallest particles. Note that applying the same morphological operations to the synthetic images did not improve the agreement between the synthetic and binarized images.

Table 4. Intersection over union area for simulated and binarized particles of different sizes.

Particle radius size (mm)	IoU
0.39 mm	0.92
0.50 mm	0.95
0.79 mm	0.97
1.59 mm	0.97

A new training dataset was generated to retrain CNN^{ϕ} considering only four particles sizes to mimic the experimental conditions. The distributions of $\hat{\phi}$ values obtained are shown in Figure 7 in separate boxplots for each volume fraction (hold-up).

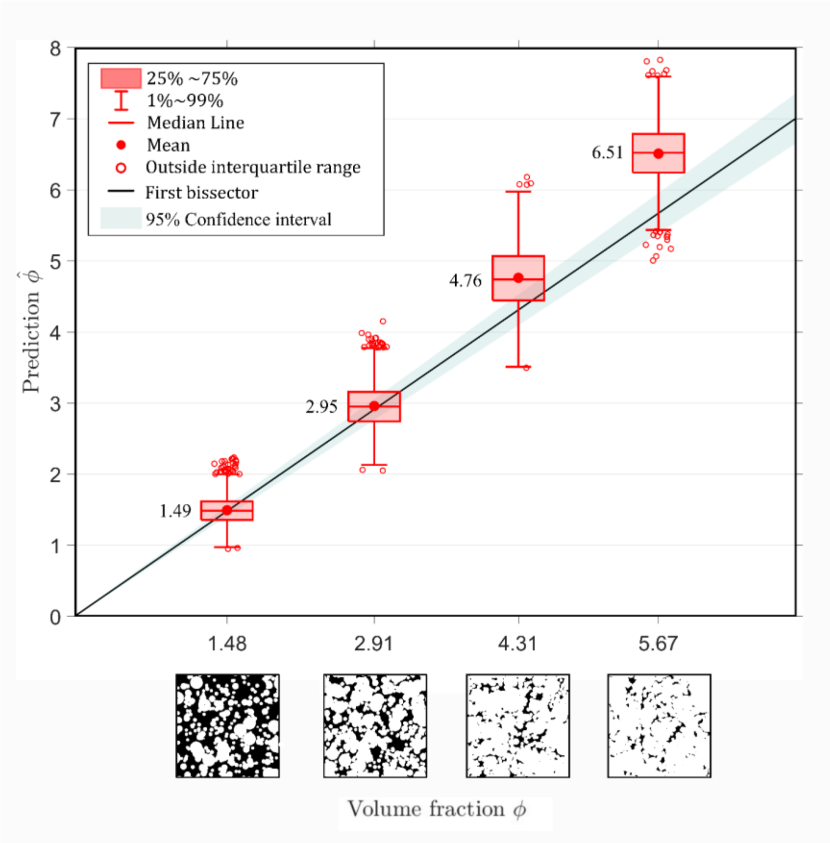

Figure 7. Boxplot representations of the distribution of predicted hold-up values obtained for each experimental particle volume fraction. Examples of the experimental images are shown below the corresponding hold-up value. Each boxplot consists of a red box extending from the first (Q_1) to the third (Q_3) quartile of the distribution and whiskers extending to $1.5 \times [Q_3 - Q_1]$. Outlier values beyond this range are shown as scattered points. The first bisector (solid line) and 95% confidence interval (shaded area) are shown to visualize the differences between the average prediction (numerical value on the left of each box) to the corresponding experimental hold-up ϕ.

These results indicate that the chosen approach was effective for all experimental images. As observed in the numerical experiments, the predictions tend to become less reliable when the particle density in the image increases. Whereas more than 25% of the predictions fell within the confidence interval at $= 1.48\%$, this proportion decreased to $12\%, 6\%$ and finally 1% at volume fractions of 2.91%, 4.31% and 5.67%, respectively. Moreover, Table 5 shows that while the relative error was within the confidence interval ($RE \leq 0.05$) for the first two experiments, the errors were an order of magnitude larger at higher volume fractions. Figure 8 compares the predicted PSDs with the ground truth for the same four experiments.

Table 5. Comparison between the average predicted value of the volume fraction ($\hat{\phi}$) and the actual value (ϕ); std, standard deviation; RE, relative error; MAE, mean absolute error.

Experiments	ϕ (%)($\pm$ scale error)	Average surface fraction (s/S)	$\hat{\phi}$ (%) ($\pm$ std)	RE	MAE ($\pm$ std)
1	1.48 ± 0.002	45.6%	1.49 ± 0.19	0.008	0.15 ± 0.12
2	2.91 ± 0.003	71.8%	2.95 ± 0.31	0.017	0.25 ± 0.19
3	4.31 ± 0.005	85.4%	4.76 ± 0.44	0.105	0.52 ± 0.37
4	5.67 ± 0.006	92.4%	6.51 ± 0.39	0.148	0.84 ± 0.38

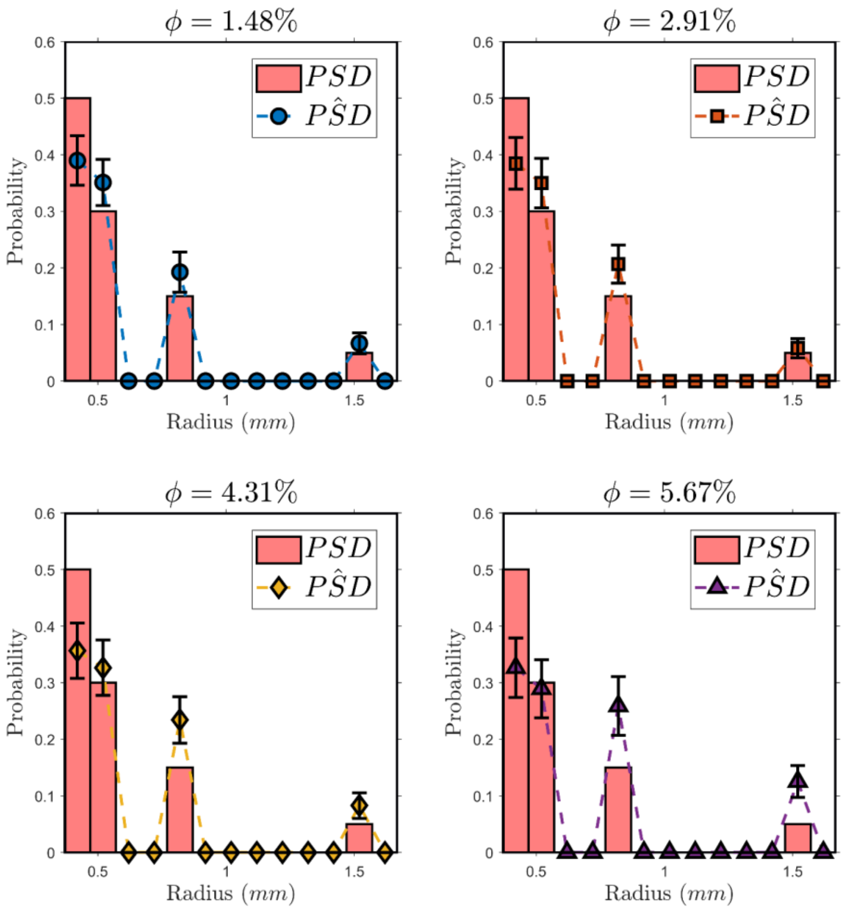

Figure 8. Comparison of predicted particle size distributions $(\widehat{PSD})$ with the ground truth (PSD) for the four considered particle volume fractions ϕ.

Figure 8 shows that at the two lower volume fractions considered, the CNN correctly recovered the PSD with only a slight underestimation of the proportion of smallest particles, probably because of the imperfections of the binarization procedure. At higher volume fractions, the PSD was not accurately recovered, the proportion of larger particles being overestimated, presumably because of particle overlap. The poorer agreement with the actual PSDs at higher particle volume fractions is reflected by an increase in the corresponding $\overline{\mathrm{MAE}}$s (Table 6).

Table 6. $\overline{MAE}$ for the four experimental PSD prediction.

Experiment	$\overline{\mathrm{MAE}}$ ($\pm$std)
1	0.018 ± 0.006
2	0.019 ± 0.006
3	0.024 ± 0.068
4	0.031 ± 0.008

4.2.Validation for a liquid-liquid system

The approach was further validated using previously acquired data (Amokrane et al., 2014). Images of water droplets in a emulsion with tetra-propylene hydrogen (TPH, density $\rho = 760$ kg/m^3; viscosity $\eta = 1.26 \times 10^{-3}$ Pa $\cdot$ s; surface tension $\gamma = 43 \times 10^{-3}$ N/m) were obtained using an in-situ video camera placed inside a cylindrical stirred tank reactor (internal volume, 1 L; internal height, H; Figure 9 (b)). Emulsions with hold-ups of up to 5% were stirred at 500 rpm with a three-flat-blade propeller (diameter, 60 mm) placed $H/3$ above the base of the vessel. Images were acquired after 60 min of stirring to ensure that a steady state had been reached.

The probe consisted of a CCD camera with LED back lighting (Figure 9 (a)). Images were obtained of the emulsion flowing through a 1500 μm wide gap between the LED and the lens. The images were 710×480 px^2 in size with a resolution of 2 μm/px allowing the detection of droplets larger than 8 μm in diameter. The images were then split into two 480×480 px^2 square images (Figure 9 (c)); to double the number of acquired images. Further information on the experimental setup and the fluids can be found in Khalil et al. (Khalil et al., 2010).

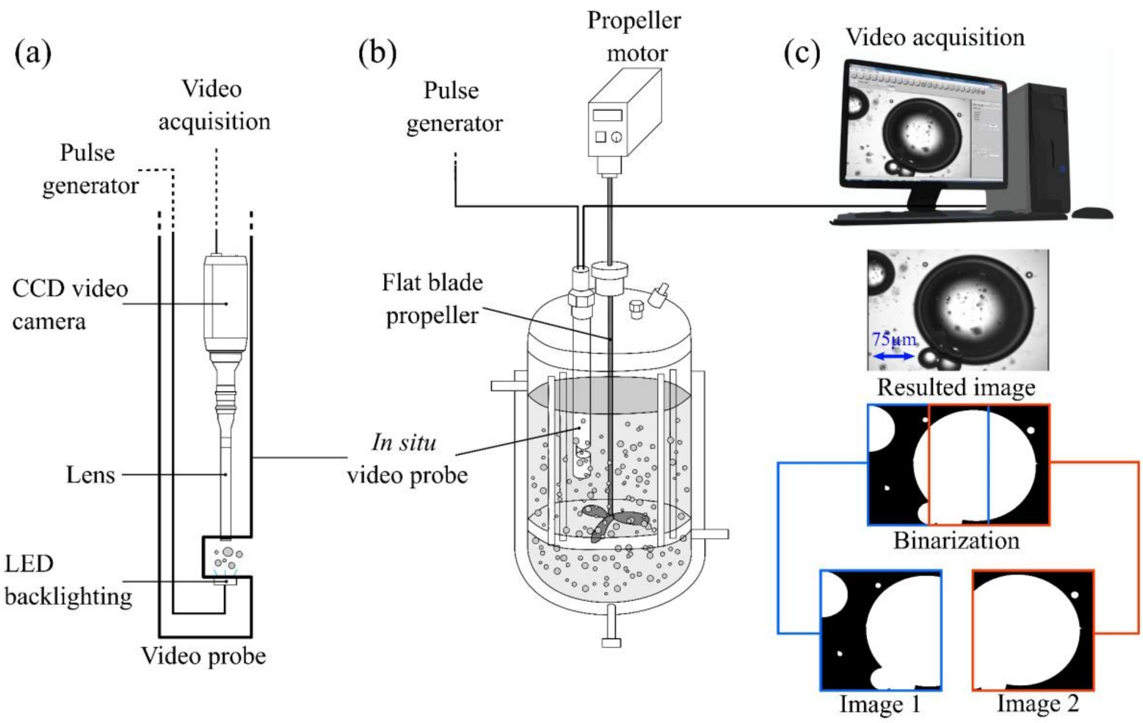

Figure 9. Schematic diagrams of the setup used to obtain images of a water-in-TPH emulsion. (a) Diagram of the video probe used to capture the images of the emulsion flowing through the gap between the lens and the LED. (b) Diagram of the double-jacketed cylindrical tank containing the emulsion, the video probe and the propeller used to stir the mixture. (c) Examples of the raw images obtained, after binarization, and after cropping.

The volume fraction and the PSD were retrieved from 3 870 images. In this experiment, the volume fraction could be controlled but the PSD of the dispersed phase was unknown. The predicted PSDs were therefore compared with values obtained by the Hough transform (Amokrane et al., 2014). The two machine learning networks, CNN^{ϕ} and $\mathrm{CNN}^{\mathrm{PSD}}$, were retrained on a new simulated dataset corresponding to the experimental setup, consisting of 240×240 pixel images in three channels ($240 \times 240 \times 3$ px^3) as before.

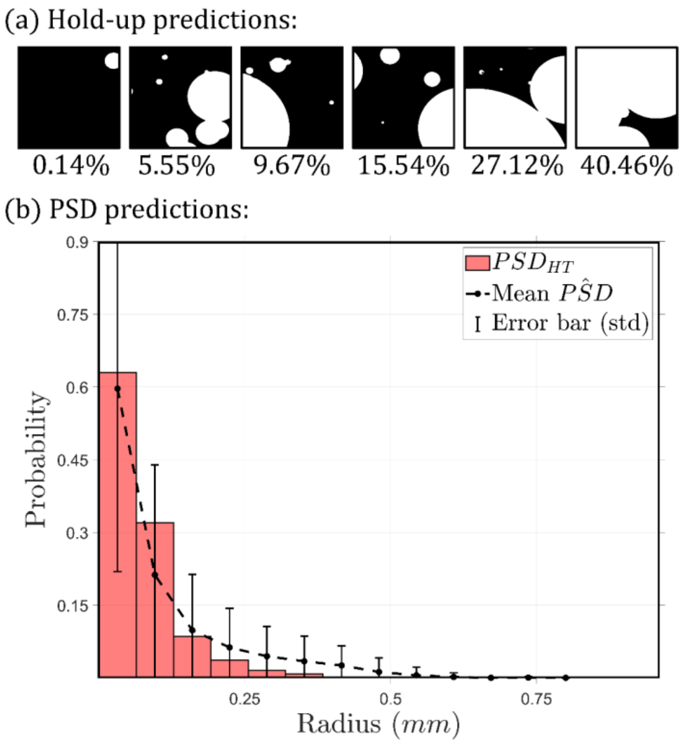

Figure 10. Validation results for a liquid–liquid system (water-in-TPH emulsion). (a) Examples of the predicted volume fraction for different experimental volume fractions (the droplet density in the images), (b) Comparison of predicted and Hough transform PSDs ($\widehat{PSD}$ vs $\mathrm{PSD_{HT}}$).

Figure 10 (a) shows the predicted hold-up values obtained beneath corresponding experimental images. The values are consistent with the actual number of droplets over a wide range of hold-up values. The mean predicted hold-up of 4.74% is in agreement with the expected value of 5% ($\mathrm{RE} = 0.052$). Figure 10 (b) compares the mean predicted PSD computed from the 3 870 images to the distribution obtained using the Hough transform. The two distributions match closely ($\overline{\mathrm{MAE}} = 0.012 \pm 0.047$), but the CNN predicts greater proportions of larger particles, suggesting that it performs better than the HT for large particles and particles that intersect with the image boundaries.

5. Conclusion and perspectives

This article describes a new image processing technique for dense flow imaging, combining a stochastic geometrical model with convolutional neural networks to retrieve 3D properties of particle systems using only 2D projected images. Using this approach, the volume fraction of the dispersed phase and the particle size distribution are predicted directly from the images. A stochastic model was developed to generate training images labeled with the targeted 3D properties of the system. Two CNN architectures were built, one to quantify the volume fraction of the observed particle field and the other to recover the PSD. After numerical validation on simulated images, the approach was validated on experimental images of calibrated beads and of an emulsion in a tank. Results confirm that average 3D quantities can be measured using this approach from a single optical access, even for flows with high-dispersed phase volume fractions. In particular, this new approach remains effective in the presence of high particle overlap, where traditional image-processing techniques typically fail. The approach is also computationally efficient, with the analysis of thousands of images typically completed in less than 30 min. Moreover, the method is easy to implement and can readily be re-purposed by transfer learning to study different types of multiphase flows, making it suitable for many applications in chemical engineering. These encouraging results highlight the value of combining a stochastic geometry model with deep learning to predict 3D information. Note that while a lognormal function was used for the PSD in this study, the model can be trained to predict any type of discrete distribution. The model could also be extended to study ellipsoidal particles, which are more representative of gas-liquid flow. This should be relatively straightforward since Matern type II models for ellipsoidal shapes have already been described in the literature (de Langlard et al., 2018b).

Future work will focus in the short term on improving the stochastic model by including spatial heterogeneity and more complex shapes (e.g. cap-shaped or skirted particles); to better account for spatial inhomogeneities in the flow images and the variety of particle shapes typically encountered in dispersed phases of multiphase flows. Also, more complex CNN architectures will be studied in order to improve the results and treat irregular shapes (Ma et al., 2022; Murata et al., 2020).

List of symbols and abbreviations

Symbols

W	Observation window (m^2)
l	Length of the projection direction (m)
r_i	Radius of the ith particle
t_i	Time of birth of the ith particle
n_p	Total number of particles
n	Number of outputs for CNN^{PSD}

N_t	Number of training images
N_v	Number of validation images
N_e	Number of testing images
N	Total number of generated images ($N = N_t + N_v + N_e$)
$\mathcal{L}_{tr}$	Truncated Lognormal law
a	First support of the truncated law
b	Second support of the truncated law
n_j	Number of particles in the jth class
d_j	Diameter of the jth class (m)
v_i	Total volume of the dispersed phase in the ith image (m^3)
V_i	Total volume of the mixture in the ith image (m^3)
ϕ_i	Volume fraction of the ith image
$\hat{\phi}_i$	Predicted volume fraction of the ith image
PSD_i	Particle size distribution of the ith image
$P\hat{S}D_i$	Predicted particle size distribution of the ith image
s^2	Variance
$\bar{d}$	Mean diameter (m)
A	Synthetic particle image
$\check{A}$	Binarized particle image
s/S	Surface fraction
$\overline{\mathrm{MAE}}$	Overall Mean Absolute Error

Greek Symbols

γ	Surface tension (N/m)
η	Viscosity (Pa.s)
λ	Point process intensity
μ, σ	Lognormal parameters
ρ	Density (kg/m^3)
ϕ	Hold-up or Volume fraction of the dispersed phase

Abbreviations

3D	Three-dimensional
2D	Two-dimensional
CNN	Convolutional Neural Network
CNN^{Φ}	Network for predicting volume fraction
$\mathrm{CNN}^{\mathrm{PSD}}$	Network for predicting particle size distribution
DL	Deep Learning
DIH	Digital In-line Holography
FC layer	Fully Connected layer
FIB-SEM	Focused Ion Beam-Scanning Electron Microscope
FBRM	Focused Beam Reflectance Measurement
MAE	Mean Absolute Error
OMAE	Global Mean Absolute Error
PMMA	Poly (Methyl Methacrylate)
PSD	Particle Size Distribution
RE	Relative Error
std	Standard Deviation
IoU	Intersection over Union

References

Acevedo, D., Wu, W.L., Yang, X., Pavurala, N., Mohammad, A., O'Connor, T.F., 2021. Evaluation of focused beam reflectance measurement (FBRM) for monitoring and predicting the crystal size of carbamazepine in crystallization processes. CrystEngComm 23, 972–985. https://doi.org/10.1039/d0ce01388a

Amokrane, A., Charton, S., Sheibat-Othman, N., Becker, J., Klein, J.P., Puel, F., 2014. Development of a CFD-PBE coupled model for the simulation of the drops behaviour in a pulsed column. Can. J. Chem. Eng. 92, 220–233. https://doi.org/10.1002/cjce.21933

Black, D.L., McQuay, M.Q., Bonin, M.P., 1996. Laser-based techniques for particle-size measurement: A review of sizing methods and their industrial applications. Prog. Energy Combust. Sci. 22, 267–306. https://doi.org/10.1016/S0360-1285(96)00008-1

Boxall, J.A., Koh, C.A., Sloan, E.D., Sum, A.K., Wu, D.T., 2010. Measurement and Calibration of Droplet Size Distributions in Water-in-Oil Emulsions by Particle Video Microscope and a Focused Beam Reflectance Method. Ind. Eng. Chem. Res. 49, 1412–1418. https://doi.org/10.1021/ie901228e

Chen, Q., Yang, X., Petriu, E.M., 2004. Watershed segmentation for binary images with different distance transforms. Proc. - 3rd IEEE Int. Work. Haptic, Audio Vis. Environ. their Appl. - HAVE 2004 111–116. https://doi.org/10.1109/have.2004.1391891

Clift, R., Grace, J. R., & Weber, M.E., 2005. Bubbles, drops, and particles.

Couto, H.J.B., Nunes, D.G., Neumann, R., França, S.C.A., 2009. Micro-bubble size distribution measurements by laser diffraction technique. Miner. Eng. 22, 330–335. https://doi.org/10.1016/j.mineng.2008.09.006

Cui, Y., Li, C., Zhang, W., Ning, X., Shi, X., Gao, J., Lan, X., 2022. A deep learning-based image processing method for bubble detection, segmentation, and shape reconstruction in high gas holdup sub-millimeter bubbly flows. Chem. Eng. J. 449, 137859. https://doi.org/10.1016/j.cej.2022.137859

Darakis, E., Khanam, T., Rajendran, A., Kariwala, V., Naughton, T.J., Asundi, A.K., 2010. Microparticle characterization using digital holography. Chem. Eng. Sci. 65, 1037–1044. https://doi.org/10.1016/j.ces.2009.09.057

de Langlard, M., Al-Saddik, H., Charton, S., Debayle, J., Lamadie, F., 2018a. An efficiency improved recognition algorithm for highly overlapping ellipses: Application to dense bubbly flows. Pattern Recognit. Lett. 101, 88–95. https://doi.org/10.1016/j.patrec.2017.11.024

de Langlard, M., Lamadie, F., Charton, S., Debayle, J., 2018b. A 3D stochastic model for geometrical characterization of particles in two-phase flow applications. Image Anal. Stereol. 37, 233–247. https://doi.org/10.5566/ias.1942

Dia, K., Lamadie, F., Debayle, J., 2022. Using deep learning to retrieve 3D geometrical characteristics of a particle field from 2D projected images: Application to multiphase flows, in: 2022 12th International Conference on Pattern Recognition Systems (ICPRS). IEEE, pp. 1–7. https://doi.org/10.1109/ICPRS54038.2022.9854059

Emmerich, J., Tang, Q., Wang, Y., Neubauer, P., Junne, S., Maaß, S., 2019. Optical inline analysis and monitoring of particle size and shape distributions for multiple applications: Scientific and industrial relevance. Chinese J. Chem. Eng. 27, 257–277. https://doi.org/10.1016/j.cjche.2018.11.011

Fend, C., Moghiseh, A., Redenbach, C., Schladitz, K., 2021. Reconstruction of highly porous structures from FIB-SEM using a deep neural network trained on synthetic images. J. Microsc. 281, 16–27. https://doi.org/10.1111/jmi.12944

Gianinoni, I., Golinelli, E., Melzi, G., Musazzi, S., Perini, U., Trespidi, F., 2003. Optical particle sizers for on-line applications in industrial plants. Opt. Lasers Eng. 39, 141–154. https://doi.org/10.1016/S0143-8166(01)00090-2

Haas, T., Schubert, C., Eickhoff, M., Pfeifer, H., 2020. BubCNN: Bubble detection using Faster RCNN and shape regression network. Chem. Eng. Sci. 216, 115467. https://doi.org/10.1016/j.ces.2019.115467

Heath, A.R., Fawell, P.D., Bahri, P.A., Swift, J.D., 2002. Estimating Average Particle Size by Focused Beam Reflectance Measurement (FBRM). Part. Part. Syst. Charact. 19, 84. https://doi.org/10.1002/1521-4117(200205)19:2<84::AID-PPSC84>3.0.CO;2-1

Heinrich, J., Ulrich, J., 2012. Application of Laser-Backscattering Instruments for In Situ Monitoring of Crystallization Processes - A Review. Chem. Eng. Technol. 35, 967–979. https://doi.org/10.1002/ceat.201100344

Honkanen, M., Eloranta, H., Saarenrinne, P., 2010. Digital imaging measurement of dense multiphase flows in industrial processes. Flow Meas. Instrum. 21, 25–32. https://doi.org/10.1016/j.flowmeasinst.2009.11.001

Huang, X., Kakuda, Y., Cui, W., 2001. Hydrocolloids in emulsions: Particle size distribution and interfacial activity. Food Hydrocoll. 15, 533–542. https://doi.org/10.1016/S0268-005X(01)00091-1

Iqbal, H., 2018. PlotNeuralNet. https://doi.org/10.5281/zenodo.2526396

Juliá, J.E., Harteveld, W.K., Mudde, R.F., Van Den Akker, H.E.A., 2005. On the accuracy of the void fraction measurements using optical probes in bubbly flows. Rev. Sci. Instrum. 76. https://doi.org/10.1063/1.1862192

Karn, A., Ellis, C., Arndt, R., Hong, J., 2015. An integrative image measurement technique for dense bubbly flows with a wide size distribution. Chem. Eng. Sci. 122, 240–249. https://doi.org/10.1016/j.ces.2014.09.036

Kavanaugh, M.C., Tate, C.H., Trussell, A.R., Trussell, R.R., Treweek, G., 1980. Use of particle size distribution measurements for selection and control of solid/liquid separation processes. Part. Water Charact. Fate, Eff. Removal, M.C. Kavanaugh; J.O. Leckie (Eds.), Washington, D.C., 305–328. https://doi.org/10.1021/ba-1980-0189.ch014

Khalil, A., Puel, F., Chevalier, Y., Galvan, J.M., Rivoire, A., Klein, J.P., 2010. Study of droplet size distribution during an emulsification process using in situ video probe coupled with an automatic image analysis. Chem. Eng. J. 165, 946–957. https://doi.org/10.1016/j.cej.2010.10.031

Kim, Y., Park, H., 2021. Deep learning-based automated and universal bubble detection and mask extraction in complex two-phase flows. Sci. Rep. 11, 8940. https://doi.org/10.1038/s41598-021-88334-0

Lamadie, F., Bruel, L., Himbert, M., 2012. Digital holographic measurement of liquid-liquid two-phase flows. Opt. Lasers Eng. 50, 1716–1725. https://doi.org/10.1016/j.optlaseng.2012.07.010

Lau, Y.M., Deen, N.G., Kuipers, J.A.M., 2013. Development of an image measurement technique for size distribution in dense bubbly flows. Chem. Eng. Sci. 94, 20–29. https://doi.org/10.1016/j.ces.2013.02.043

Li, J., Shao, S., Hong, J., 2021. Machine learning shadowgraph for particle size and shape characterization. Meas. Sci. Technol. 32. https://doi.org/10.1088/1361-6501/abae90

Ma, L., Kashanj, S., Xu, S., Zhou, J., Nobes, D.S., Ye, M., 2022. Flow Reconstruction and Prediction Based on Small Particle Image Velocimetry Experimental Datasets with Convolutional Neural Networks. Ind. Eng. Chem. Res. 61, 8504–8519. https://doi.org/10.1021/acs.iecr.1c04704

Maaß, S., Wollny, S., Voigt, A., Kraume, M., 2011. Experimental comparison of measurement techniques for drop size distributions in liquid/liquid dispersions. Exp. Fluids 50, 259–269. https://doi.org/10.1007/s00348-010-0918-9

Matérn, B., 2014. Spatial Variation, Encyclopedia of Environmental Change. https://doi.org/10.4135/9781446247501.n3658

Murata, T., Fukami, K., Fukagata, K., 2020. Nonlinear mode decomposition with convolutional neural networks for fluid dynamics. J. Fluid Mech. 882, 1–15. https://doi.org/10.1017/jfm.2019.822

Panckow, R.P., Reinecke, L., Cuellar, M.C., Maaß, S., 2017. Photo-Optical In-Situ Measurement of Drop Size Distributions: Applications in Research and Industry. Oil Gas Sci. Technol. – Rev. d'IFP Energies Nouv. 72, 14. https://doi.org/10.2516/ogst/2017009

Pandalaneni, K., Amamcharla, J.K., 2016. Focused beam reflectance measurement as a tool for in situ monitoring of the lactose crystallization process. J. Dairy Sci. 99, 5244–5253. https://doi.org/10.3168/jds.2015-10643

Pandit, A., Katkar, V., Ranade, V., Bhambure, R., 2019. Real-Time Monitoring of Biopharmaceutical Crystallization: Chord Length Distribution to Crystal Size Distribution for Lysozyme, rHu Insulin, and Vitamin B12. Ind. Eng. Chem. Res. 58, 7607–7619. https://doi.org/10.1021/acs.iecr.8b04613

Poelma, C., 2020. Measurement in opaque flows: a review of measurement techniques for dispersed multiphase flows. Acta Mech. 231, 2089–2111. https://doi.org/10.1007/s00707-020-02683-x

Ruf, A., Worlitschek, J., Mazzotti, M., 2000. Modeling and Experimental Analysis of PSD Measurements through FBRM. Part. Part. Syst. Charact. 17, 167–179. https://doi.org/10.1002/1521-4117(200012)17:4<167::AID-PPSC167>3.0.CO;2-T

Sentis, M.P.L., Bruel, L., Charton, S., Onofri, F.R.A., Lamadie, F., 2017. Digital in-line holography for the characterization of flowing particles in astigmatic optical systems. Opt. Lasers Eng. 88, 184–196. https://doi.org/10.1016/j.optlaseng.2016.08.012

Shao, S., Mallery, K., Hong, J., 2020. Machine learning holography for measuring 3D particle distribution. Chem. Eng. Sci. 225. https://doi.org/10.1016/j.ces.2020.115830

Sheng, J., Malkiel, E., Katz, J., 2006. Digital holographic microscope for measuring three-dimensional particle distributions and motions. Appl. Opt. 45, 3893–3901. https://doi.org/10.1364/AO.45.003893

Stoyan, D., Stoyan, H., 1985. On One of Matérn’s Hard-core Point Process Models. Math. Nachrichten 122, 205–214. https://doi.org/10.1002/mana.19851220121

Suh, Y., Bostanabad, R., Won, Y., 2021. Deep learning predicts boiling heat transfer. Sci. Rep. 11, 1–10. https://doi.org/10.1038/s41598-021-85150-4

Wang, H.Y., Shi, Y.F., Zhu, X.J., Song, L.M., Dong, F., 2022. 3-D Reconstruction of Bubble Flow Field Based on the Method of Multivision by Rough-Precise Location Algebraic Reconstruction Technique. IEEE Trans. Instrum. Meas. 71. https://doi.org/10.1109/TIM.2022.3158993

Xue, T., Qu, L., Wu, B., 2014. Matching and 3-D reconstruction of multibubbles based on virtual stereo vision. IEEE Trans. Instrum. Meas. 63, 1639–1647. https://doi.org/10.1109/TIM.2013.2289586

Yang, Y., Kang, B.S., 2011. Digital particle holographic system for measurements of spray field characteristics. Opt. Lasers Eng. 49, 1254–1263. https://doi.org/10.1016/j.optlaseng.2011.06.017

Yu, X., Xing, D., Hazuku, T., Takamasa, T., Ishimaru, T., Tanaka, Y., Akiba, T., 2009. Measurement technique for solid-liquid two-phase flow using a Normal-line Hough Transform method. J. Phys. Conf. Ser. 147, 012053. https://doi.org/10.1088/1742-6596/147/1/012053

Zafari, S., Murashkina, M., Eerola, T., Sampo, J., Kälviäinen, H., Haario, H., 2020. Resolving overlapping convex objects in silhouette images by concavity analysis and Gaussian process. J. Vis. Commun. Image Represent. 73, 102962. https://doi.org/10.1016/j.jvcir.2020.102962

Zhang, W.H., Jiang, X., Liu, Y.M., 2012. A method for recognizing overlapping elliptical bubbles in bubble image. Pattern Recognit. Lett. 33, 1543–1548. https://doi.org/10.1016/j.patrec.2012.03.027

Zou, T., Pan, T., Taylor, M., Stern, H., 2021. Recognition of overlapping elliptical objects in a binary image. Pattern Anal. Appl. 24, 1193–1206. https://doi.org/10.1007/s10044-020-00951-z